Numerical Simulations of the Moisture Movement in Unsaturated Bentonite Under a Thermal Gradient

J. W. Park, K. Chang, and C. L. Kim

Korea Electric Power Corporation
150 Dukjin-dong, Yusong-gu, Taejon, 305-353, Korea
p5j9w@kepco.co.kr

Abstract

The one-dimensional finite element program was developed to analyze the coupled behavior of heat, moisture, and air transfer in unsaturated porous media. By using this program, the simulation results were compared with those from the laboratory infiltration tests under isothermal condition and temperature gradient condition, respectively. The discrepancy of water uptake was found in the upper region of a bentonite sample under isothermal condition between numerical simulation and laboratory experiment. This indicated that air pressure was built up in the bentonite sample which could retard the infiltration velocity of liquid. In order to consider the swelling phenomena of compacted bentonite which cause the discrepancy of the distribution of water content and temperature, swelling and shrinkage factors were incorporated into the finite element formulation. It was found that these factors could be effective to represent the moisture diffusivity and unsaturated hydraulic conductivity due to volume change of bentonite sample.

1. Introduction

Taking into consideration of the real situation in a deep geological repository, the buffer material will be likely to remain unsaturated for an extended period of time while the water table returns slowly to its natural level after sealing of the repository. Bentonite as a buffer material, within which decay heat from wastes is generated on one side whilst groundwater from host-rock flows into the other side, will undergo the simultaneous heating and hydration in the early stage of waste emplacement. The soil-water interaction under a temperature gradient in bentonite will have an influence on the integrity and performance of the overall engineered barrier system. Since infiltration is a two-phase process with air being displaced by the infiltrating water,

the effect of the air is also not negligible in certain circumstances. Air may be swept in front of the wetting front by increasing the air pressure on the water menisci. In the meantime, shortly after the emplacement of waste, bentonite can undergo thermal drying, shrinkage and cracking near the waste package. It has long been recognized that clay soil showed the hydrological problems which were not found for non-swelling soils. For swelling clays, which contain water and air, their intrinsic permeabilities are not equal because the pore structure of a dry clay soil is completely different from that of a water-saturated clay sample even at the same dry density. In this context, experimental and theoretical investigations on this heat-induced moisture movement in compacted bentonite have the significance to understand the physical processes occurring during water resaturation period.

From the literature review, a model based on the Philip and de Vries equations[1] for non-isothermal moisture movement and heat conduction would give better results to predict transient flow in bentonite buffer systems. Based on the Philip and de Vries' model, many researchers have formulated the coupled heat and moisture transfer problems for the thermo-hydraulic analysis of clay-based buffer materials used in a high-level radioactive waste repository. Extension of the heat and moisture transfer model to include the influence of the air phase was carried out by Hartley[2], Pollock[3], and Thomas and Sansom[4].

In this paper, a finite-element program for the solution of potential-based coupled heat, moisture and air transfer in unsaturated soil was developed based on the previous works. One-dimensional numerical simulations were then conducted to compare with laboratory-scale isothermal and thermal infiltration experiments. The influence of the air phase and soil swelling effect on the water

movement in bentonite was investigated. In order to consider the swelling phenomena of compacted bentonite, swelling and shrinkage factors were incorporated into the finite element formulation.

2. Coupled Heat, Moisture and Air Transfer Model

2.1. Theoretical Formulation

The model is based on combinations of equations or derivations from conservation principles and the classical laws of known physical phenomena for the coupled moisture, air and heat flow[4]. Governing differential equations for pore water, pore air and heat transfer in non-isothermal unsaturated soil are derived as follows:

Moisture transfer

Conservation of mass for liquid and vapor flow dictates that:

$$\frac{\partial(\rho_l \theta_l)}{\partial t} + \frac{\partial(\rho_v \theta_v)}{\partial t} = -\nabla \cdot (\rho_l \underline{u}) - \nabla \cdot (\rho_l \underline{v}) - \nabla \cdot (\rho_v \underline{v}_a) \quad (1)$$

where ρ_l : density of pore water[kg/m³],

ρ_v : density of water vapor[kg/m³],

θ_l : volumetric liquid content[-],

θ_v : volumetric vapor content[-],

$\underline{u}$: liquid velocity[m/sec],

$\underline{v}$: velocity of vapor flow[m/sec],

$\underline{v}_a$: air velocity[m/sec],

t : time [sec]

The movement of vapor due to vapor diffusion in addition to the air transport of vapor is considered in equation (1).

Assuming that the liquid and dry air flow are governed by generalized Darcy's law, and that the velocity of vapor flow can be given by utilizing the water vapor density expressed by the psychrometric law, liquid, vapor and air velocities are written respectively as:

$$\underline{u} = -K\nabla\psi - (\frac{K}{\gamma_w})\nabla P_a - K \qquad (2)$$

$$\underline{v} = -(K_{v1}\nabla\psi + K_{v2}\nabla T) \qquad (3)$$

$$\underline{v}_a = -(\frac{K_a k_{ra}}{\mu_a})\,\nabla P_a \qquad (4)$$

where K : unsaturated hydraulic conductivity, depending on both liquid content and the temperature of soil[m/sec],

ψ : capillary potential[Pa],

T : temperature[K],

P_a : total air pressure[Pa],

γ_w : specific weight of water[kg/m³],

K_a : intrinsic permeability of the air phase[m²],

k_{ra} : relative permeability of air phase [-] $k_{ra} = (n-\theta_l)/n$,

n : porosity[-],

μ_a : viscosity of air[N sec/m²],

$$K_{v1} = \frac{D_{atm}\,vn\rho_0 gh}{\rho_l R_v T},$$

$$K_{v2} = \frac{D_{atm}\,vn}{\rho_l}\frac{(\nabla T)_a}{\nabla T}(h\beta - \frac{\rho_0 h\psi g}{R_v T^2}),$$

ρ_0 : density of saturated water vapor [kg/m³],

h : relative humidity[-],

R_v : specific gas constant for water vapor[J/kg K],

β : thermal expansion coefficient of water $(= \dfrac{\partial\rho_0}{\partial T}$).

D_{atm} : molecular diffusivity of water vapor in air[m²/sec],

v : mass flow factor[-],

$\dfrac{(\nabla T)_a}{\nabla T}$: ratio of microscopic temperature gradient in the pore space to the macroscopic temperature gradient

In deriving equation (3), mechanistic enhancement factor introduced by Philip and de

Vries and the modification proposed by Ewen and Thomas[5] are employed herein.

Putting equations (2), (3), and (4) into equation (1), we obtain the governing differential equation for moisture flow as:

$$C_{\psi\psi}\frac{\partial\psi}{\partial t} + C_{\psi T}\frac{\partial T}{\partial t} = \nabla\cdot(K_{\psi\psi}\nabla\psi) + \nabla\cdot(K_{\psi T}\nabla T) + \nabla\cdot(K_{\psi a}\nabla P_a)$$
$$+ V_{\psi\psi}\nabla\psi + V_{\psi T}\nabla T + \nabla\cdot K \qquad (5)$$

where

$$C_{\psi\psi} = C_{l1} + C_{v1}, \quad C_{\psi T} = C_{l2} + C_{v2},$$
$$K_{\psi\psi} = K + K_{v1}, \quad K_{\psi T} = K_{v2},$$
$$K_{\psi a} = K_{l3} + K_{v3}, \quad V_{\psi\psi} = V_{v1}, \quad V_{\psi T} = V_{v2}$$

<u>Pore air mass transfer</u>

Using Henry's law to take account of dissolved air in the pore water, following equation is derived for the dry air phase from the principle of mass conservation:

$$\frac{\partial}{\partial t}[\rho_{da}(\theta_a + H_c\theta_l)] = -\nabla\cdot[\rho_{da}(\underline{v}_a + H_c\underline{u})] \quad (6)$$

where ρ_{da} : density of dry air[kg/m³],

H_c : Henry's coefficient of solubility[-]

Considering the dry air and the water vapor as ideal gas and using Dalton's law of partial pressures, the density of dry air is evaluated from:

$$\rho_{da} = \frac{P_a}{R_{da}} - \frac{\rho_v R_v}{R_{da}} \qquad (7)$$

where R_{da}: gas constant for dry air[J/kg K]

Differentiating equation (7) with respect to time and space, and making appropriate substitutions for the liquid and dry air velocity, equation (6) is written as:

$$C_{a\psi}\frac{\partial\psi}{\partial t} + C_{aT}\frac{\partial T}{\partial t} + C_{aa}\frac{\partial P_a}{\partial t} = \nabla\cdot(K_{a\psi}\nabla\psi) + \nabla\cdot(K_{aa}\nabla P_a)$$
$$+ V_{a\psi}\nabla\psi + V_{aT}\nabla T + V_{aa}\nabla P_a + \rho_{da}H_c\nabla\cdot K \quad (8)$$

where

$$C_{a\psi} = [n + (H_c - 1)\theta_l]X_{a1} + (H_c - 1)\rho_{da}C_{l1},$$
$$C_{aT} = [n + (H_c - 1)\theta_l]X_{a2} + (H_c - 1)\rho_{da}C_{l2},$$
$$C_{aa} = [n + (H_c - 1)\theta_l]X_{a3},$$

$$K_{a\psi} = \rho_{da} H_c K,$$

$$K_{aa} = \rho_{da}(\frac{K_a k_{ra}}{\mu_a}) + \frac{\rho_{da} H_c K}{\gamma_w},$$

$$V_{a\psi} = -[v_a + H_c u]X_{a1},$$

$$V_{aT} = -[v_a + H_c u]X_{a2},$$

$$V_{aa} = -[v_a + H_c u]X_{a3},$$

$$X_{a1} = -\frac{\rho_v g}{R_{da} T},$$

$$X_{a2} = -[\frac{P_a}{R_{da} T^2} + \frac{R_v h}{R_{da}}(\beta - \frac{\rho_0 \psi g}{R_v T^2})],$$

Heat transfer

Considering heat transfer by means of conduction, convection and latent heat of vaporization effects, and applying the principle of conservation of energy, following equation is derived:

$$\frac{\partial}{\partial t}\{H(T - T_r) + (n - \theta_l)\rho_v L\} = -\nabla \underline{q}_h \qquad (9)$$

where H : volumetric heat capacity for unsaturated soil, defined as:

$$H = (1 - n)\rho_s C_{ps} + \theta_l \rho_l C_{pl} + (n - \theta_l)\rho_v C_{pv} \\ + (n - \theta_l)\rho_{da} C_{pda} \qquad (10)$$

where ρ_s : density of the soil grain[kg/m^3],

C_{ps} : specific heat capacity of the soil grain[J/kg K]

The heat flux per unit area, $\underline{q}_h$, is written as:

$$q_h = -\lambda \nabla T + (\rho_l \underline{v} + \rho_v \underline{v}_a)L + (C_{pl} \rho_l u + C_{pv} \rho_l \underline{v} \\ + C_{pv} \rho_v \underline{v}_a + C_{pda} \rho_{da} \underline{v}_a)(T - T_r) \qquad (11)$$

where λ : coefficient of thermal conductivity of the unsaturated soil[W/m K],

L : latent heat of vaporization of water[J/kg],

C_{pl}, C_{pv}, C_{pda} : specific heat capacity of soil water, soil vapor and dry air,

respectively[J/kg K],

T_r : reference temperature[K]

By substituting equations (10) and (11) into equation (9) and expanding it, the governing differential equation for heat flow is expressed as:

$$C_{T\psi}\frac{\partial \psi}{\partial t} + C_{TT}\frac{\partial T}{\partial t} + C_{Ta}\frac{\partial P_a}{\partial t} = \nabla \cdot (K_{T\psi}\nabla \psi) + \nabla \cdot (K_{TT}\nabla T) \\ + \nabla \cdot (K_{aa}\nabla P_a) + V_{T\psi}\nabla \psi + V_{TT}\nabla T + V_{Ta}\nabla P_a \qquad (12) \\ + \rho_l C_{pl}(T - T_r)\nabla \cdot K$$

where

$$C_{T\psi} = (\rho_l C_{pl} - \rho_{da} C_{pda})(T - T_r)C_{l1} + C_{pda}(T - T_r)\theta_a X_{a1} \\ + \rho_l[C_{pv}(T - T_r) + L]C_{v1},$$

$$C_{TT} = H + (\rho_l C_{pl} - \rho_{da} C_{pda})(T - T_r)C_{l2} \\ + C_{pda}(T - T_r)\theta_a X_{a2} + \rho_l[C_{pv}(T - T_r) + L]C_{v2},$$

$$C_{Ta} = C_{pda}(T - T_r)\theta_a X_{a3},$$

$$K_{T\psi} = \rho_l C_{pl}(T - T_r)K_{l1} + \rho_l[C_{pv}(T - T_r) + L]K_{v1},$$

$$K_{Ta} = \rho_l \rho_{da} C_{pda}(T - T_r)K_{v3}/\rho_v + \rho_l[C_{pv}(T - T_r) + L]K_{v3} \\ + KC_l(T - T_r)$$

$$V_{T\psi} = \rho_l[C_{pv}(T - T_r) + L]V_{v1} - C_{pda}(T - T_r)V_a X_{a1},$$

$$V_{TT} = \rho_l[C_{pv}(T - T_r) + L]V_{v2} \\ - (\rho_l C_{pl}u + \rho_l C_{pv}v + \rho_v C_{pv}v_a + \rho_{da} C_{pda}v_a) \\ - C_{pda}(T - T_r)V_a X_{a2},$$

$$V_{Ta} = -C_{pda}(T - T_r)V_a X_{a3}$$

2.2. Numerical Formulation

Applying a Galerkin formulation of the finite element method derives a solution of the nonlinear partial differential equations (5), (8), and (12). The resulting systems of matrix equations are as follows:

$$[K]\{\Phi\} + [C]\{\dot{\Phi}\} + \{J\} = 0 \qquad (13)$$

where $[K] = \begin{bmatrix} K_{\psi\psi} & K_{\psi T} & K_{\psi a} \\ K_{T\psi} & K_{TT} & K_{Ta} \\ K_{a\psi} & V_{aT} & K_{aa} \end{bmatrix}$, $[C] = \begin{bmatrix} C_{\psi\psi} & C_{\psi T} & 0 \\ C_{T\psi} & C_{TT} & C_{Ta} \\ C_{a\psi} & C_{aT} & C_{aa} \end{bmatrix}$,

$$\{\Phi\} = \{\psi \ T \ P_a\}^T, \{\dot{\Phi}\} = \{\dot{\psi} \ \dot{T} \ \dot{P}_a\}^T, \{J\} = \{J_\psi \ J_T \ J_a\}^T$$

Table 1. Isothermal Infiltration Test Condition

Items	Test Condition
Sample material	Compacted bentonite
Dry density (g/cm³)	1.8
Initial water content (%)	0.0
Sample dimension (mm)	Dia. 20 × Height 20
Temperature (℃)	25
Infiltration time (hour)	2, 4, 6, 16, 24, 48, 72, 96
Infiltration solution	Distilled water

The numerical solution of equation (13) is accomplished by the use of Crank-Nicholson time-stepping scheme in which the discretized equations are replaced by:

$$\left[\frac{C}{\Delta t}+\frac{K}{2}\right]\{\Phi_{n+1}\}+\left[-\frac{C}{\Delta t}+\frac{K}{2}\right]\{\Phi_n\}+\frac{1}{2}[\{J_{n+1}\}+\{J_n\}]=0 \quad (14)$$

where   n : time level, Δt : time step size,
The algorithm is iterative, and a converged solution is deemed to be achieved when

$$|\{\Phi_{n+1}^{i+1}\}-\{\Phi_{n+1}^{i}\}|/|\{\Phi_{n+1}^{i}\}|\langle \varepsilon \quad \text{at all nodes} \qquad (15)$$

where i   : iteration number,
       ε : convergence criteria to be employed.

3. Applications

3.1. Infiltration Under Isothermal Condition

The distributions of the volumetric water content for infiltration test at constant temperature are compared with numerical results. The compacted bentonite sample, which is dried in the oven(water content 0%) at 110℃ for 24 hours, was installed in a stainless steel column. The lower part of this sample column was then put into water tank. The sample was sliced into 10 pieces after prescribed infiltration duration. The spatial water content distribution
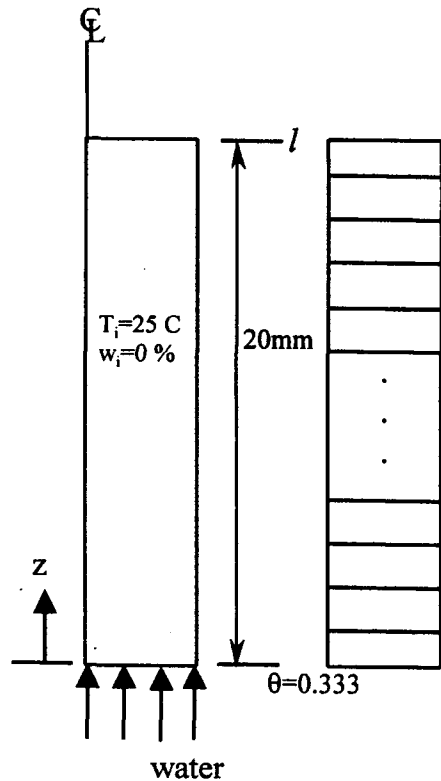

Fig. 1. Finite Element Analysis Model for Isothermal Infiltration

with prescribed infiltration periods was determined by measuring the weight of sliced samples before and after infiltration. Isothermal infiltration test conditions are summarized in Table 1. With a view to simulate the isothermal case by the coupled model, temperatures and air pressures are fixed to investigate just the variations of volumetric water content among the variables of interest. Initial and boundary conditions for this calculation are given below and illustrated in Fig. 1:

$$0\le z\le l, \quad l=0.02m$$
$$\theta=0 \qquad\qquad at \quad t=0, z>0$$
$$\frac{\partial\theta}{\partial z}=0 \qquad\quad at \quad t>0, z=l \qquad (16)$$
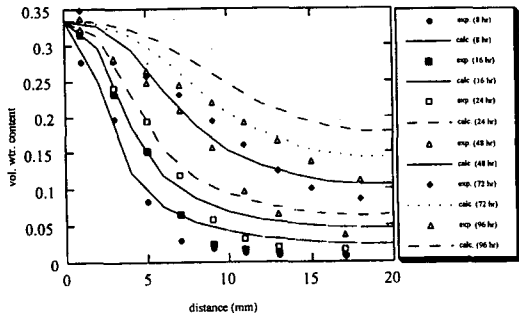$$\theta=\theta_{sat}=0.333 \quad at \quad t>0, z=0$$

Fig. 2. Comparison Between Calculated and Measured Volumetric Water Content Along the Length of the Sample (Isothermal, Coupled Model)

The capillary potential-volumetric water content relationship and the unsaturated hydraulic conductivity-volumetric water content relationship are incorporated into the numerical program as follows[6]:

$$\psi = \frac{1}{a}[(\frac{\theta - \theta_r}{\theta_s - \theta_r})^{\frac{\lambda}{1-\lambda}} - 1]^{\frac{1}{\lambda}} \qquad (17)$$

where a : -4.53E-4 [mH2O],

λ : 2.08,

θs : 0.333 ; saturated volumetric water content[-],

θ_r : 1.0E-4 ; residual volumetric water content[-]

$$K = \frac{\mu(T_r)}{\mu(T)} K_{sat} [\sqrt{S_{eff}}\{1 - (1 - S_{eff}^{\frac{1}{\lambda-1}})^{\frac{\lambda-1}{\lambda}}\}^2] \qquad (18)$$

where T_r : reference temperature, which is 20 ℃,

K_{sat}: 2.5E-14 [m/s] ; saturated hydraulic conductivity, which is an average value from the experiment at 25℃,

S_{eff}: $= \frac{S_l - S_r}{S_{ls} - S_r}$; effective degree of saturation[-]

Fig. 2 shows the volumetric water content variations as a function of distance from the
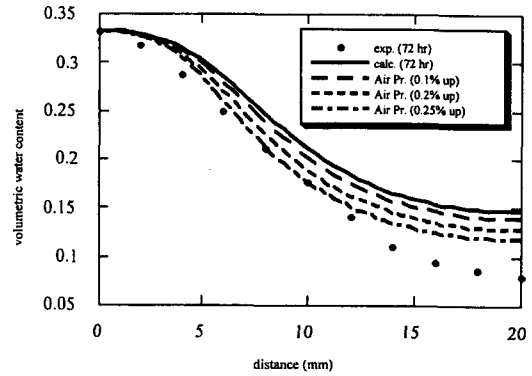

Fig. 3. Volumetric Water Content Variation with Distance in Case of Increased Air Pressure at the Upper Boundary
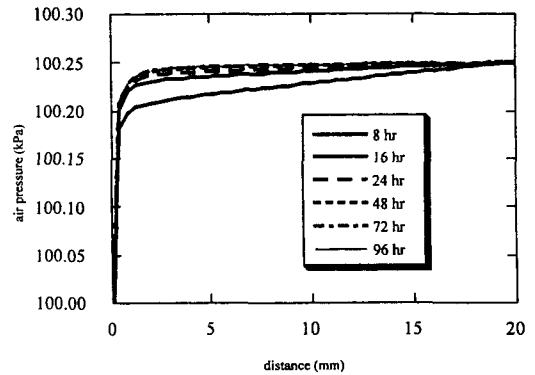

Fig. 4. Air Pressure Variation with Time Along the Sample Length

infiltration surface. It shows some discrepancy resulting in higher values in upper region of the sample than the model prediction. This means that the calculated water uptake is faster than in the experiment. As one of the probable explanations on the causes of the discrepancy, influence of induced elevated air pressures on the hydration process is considered.

The simulation results considering the assumption of the increased air pressure at the upper boundary of the column are shown in Fig. 3 and 4. Fig. 3 shows that there is a large difference in volumetric water content infiltrating

Table 2. Thermal Infiltration Test Condition

Items	Test Condition
Sample material	Compacted bentonite
Dry density (g/cm³)	1.65
Initial water content (%)	16.5
Sample dimension (mm)	Dia. 50 x Height 100
Number of samples (ea)	3 (1 for checking the uniformity of water content and dry density)
Temperature (℃)	75, 55, 35 (lower side), 25 (upper side), Temperature gradient :5,3,1 ℃ /cm

into the bentonite column among the cases of constant and elevated air pressure. The volume of water that penetrates into the bentonite column is dependent on the capillary potential in bentonite, and the capillary potential is lower at the elevated air pressure case. As expected, when the air pressure has built up, less liquid has infiltrated into bentonite. From these simulations, it is expected that the air pressure in the bentonite column would increase around 0.3%. Spatial variation of air pressure for the 0.25%-increase case in Fig. 4 shows that the model yields almost uniform pressure distributions within the sample for various simulation time frames. It is because the gas permeability used in the model is sufficiently large to enable the air pressure in the sample to be equalized throughout the column as it changes.

3.2. Infiltration Under Temperature Gradient Condition

The experimental apparatus was designed to determine the moisture and temperature distributions by imposing thermal gradient across the compacted bentonite. Two thermo-chambers were connected to the test columns to maintain constant temperatures at upper and bottom ends,
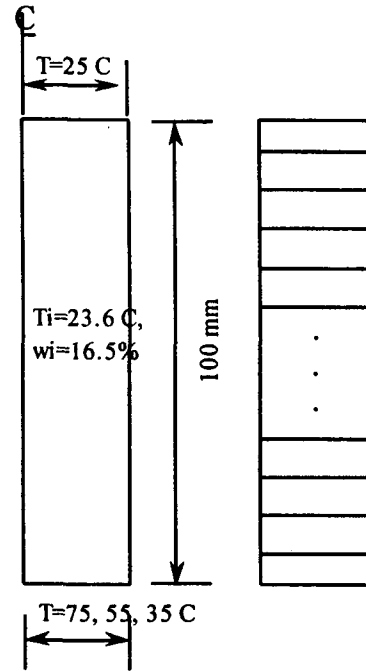

Fig. 5. Finite Element Analysis Model for Calculation of Moisture Movement Under a Temperature Gradient

respectively. In this test, two sample columns, one for temperature measurement and the other for water content measurement, were used. Six K-type thermocouples along the column and data logging system were installed to obtain the time-dependent temperature distribution. The moisture distribution was determined according to the same procedure as the isothermal infiltration test. Test conditions are summarized in Table 2. In the numerical simulation, different temperatures are applied to each end of bentonite samples to give the temperature gradient of 1, 3 and 5℃/cm. The finite element model employed is shown in Fig. 5, and the problem definitions are given as:

$$0 \leq z \leq l, \quad l = 0.1m$$

$$\psi_i = -744.0 \ mH_2O, \quad T_i = 23.6°C, \quad P_{ai} = 100 \ kP_a \ at \ t = 0, 0 \leq z \leq l$$

$$u = 0, v = 0, v_a = 0, \quad T_L = 25.0°C, \quad P_a = 100 \ kP_a \ at \ t)0, z = l \quad (19)$$

$$u = 0, v = 0, v_a = 0, \quad T_H = 75.0°C, \quad P_a = 100 \ kP_a \ at \ t)0, z = 0$$
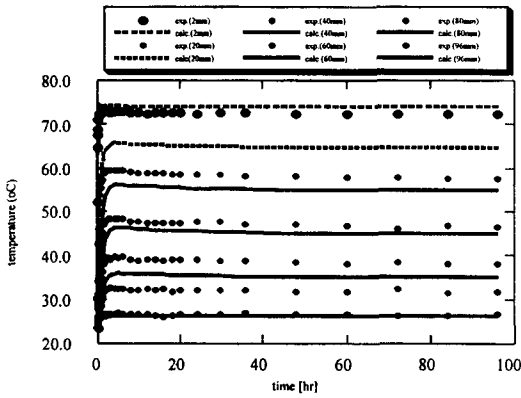
Fig. 6. Comparison Between Calculated and Measured Temperature Distributions (Temp. Diff. =5 ℃/cm Case)

Fig. 7. Comparison Between Calculated and Measured Water Content Distributions Along the Sample Length at 96Hour (0 cm: Hot Side, 10 cm: Cold Side)

The thermal properties such as specific heat capacity and thermal conductivity of the bentonite in this simulation are obtained from Kanno et al.[7].

The experimental and numerical results on the temperature variations with time at different elevations are compared in Fig. 6. The experimental temperature distribution for both upper and bottom ends show good agreement with the calculated temperature distribution, while those for other elevations are higher temperature distributions than experimental ones. The water content distribution at 96 hour is shown in Fig. 7. Both calculated and experimental results shown in this figure indicate the water movement in the bentonite sample from the hotter region to the colder. This is in accordance with physically realistic behavior because the capillary potential gradients act in this direction inducing liquid flow from the wetter region into the drier region. The overall patterns of temperature and water content distributions show the general qualitative trends and applicability of the mechanistic models, as the program used herewith, to reproduce the experimental results.

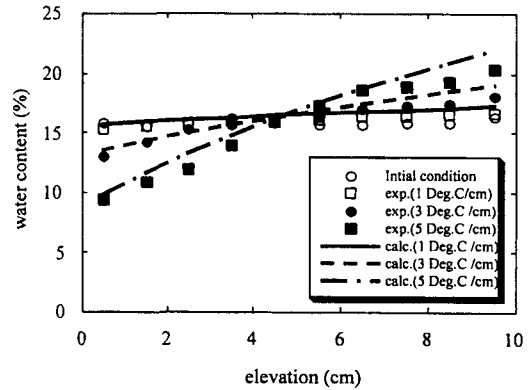One of the discrepancies between the calculated

and the measured values is thought to be from the effect of swelling. Previous researchers also concluded that uncertainty of the estimates for the material properties is undoubtedly responsible for the swelling effect peculiar to the highly compacted bentonite[6,7,8]. Therefore, a certain constitutive relationships to describe the swelling phenomena is needed and it should be incorporated the numerical formulations. Consequently, the formulated model to be desired will be the coupled thermo-hydraulic-mechanical model which could accommodate the deformation characteristics of bentonite. However, very limited data are available to complete the desired model at present.

As one possibility to accommodate the swelling and shrinkage effects on highly compacted bentonite into partially coupled model, i.e. thermo-hydraulic model prior to the final thermo-hydro-mechanical modeling, simple swelling and shrinkage factors are introduced to account for the reduced cross-sectional area for vapor flow caused by water and solid expansion of the bentonite. This approach is based on the observation and inference proposed by Nakano et al.[9] which describes the moisture movement trends
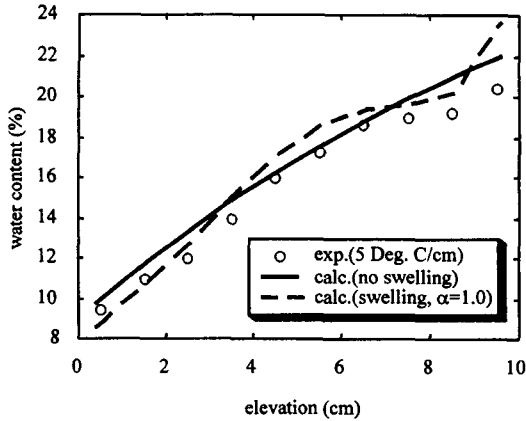
Fig. 8. Comparison Between Calculated and Measured Water Content Along the Length of the Sample Considering Swelling Effect (Test Condition:ρ_d=1.65 g/cm^3, ω_i=16.5 %, n=0.389, T$_l$=25℃, T$_h$=75℃, t=96 hr)
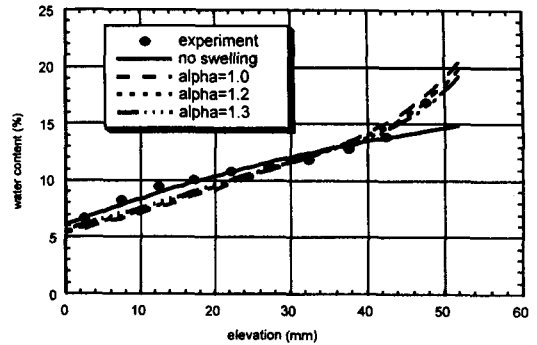

Fig. 9. Comparison Between Calculated and Measured Water Content Along the Length of the Sample Considering Swelling Effect (Test condition : ρ_d=1.8 g/cm^3, ω_i=11.1%, n=0.333, T$_l$=30℃, T$_h$=60℃, t=148 hr; from Reference [7])

considering microscopic structure of bentonite. According to their experiments on isothermal infiltration into an unsaturated swelling bentonite, it was found that water diffusivity distributions with volumetric water content in highly compacted bentonite could be represented as a U-form curve. It showed the moisture movement trends that water vapor was more active in the lower water content region and that water liquid movement became active in the high water content region. It is therefore assumed that swelling and shrinkage factors can be introduced not to directly describe the change of porosity, but to represent the degree of influence on the change of moisture diffusivity and unsaturated hydraulic conductivity due to the volume change in bentonite sample. Both swelling factor (f_{sw}) and shrinkage factor (f_{sh}) are assumed to be depended on the volumetric water content and temperature. And the functional dependency of these two factors is approximated as a diffusion process in which they represent the respective extent of contribution of liquid diffusivity ($D_{\theta l}$) and vapor diffusivity ($D_{\theta v}$) to total diffusivity ($D_\theta = D_{\theta l} + D_{\theta v}$) in the following

forms:

$$f_{sw} = D_{\theta l} / D_\theta \cdot n^\alpha,$$
$$f_{sh} = D_{\theta v} / D_\theta \cdot n^\alpha \qquad (20)$$

where n : porosity of bentonite, α : exponent Here these diffusivities can be obtained by applying Philip and de Vries' equation to water vapor diffusivity and Darcy's equation to liquid water diffusivity under isothermal condition[6]. Equation (20) means that the value of swelling factor increases as the volumetric water content increases because the influence of water vapor movement on water diffusivity diminishes. By relating these factors to permeability, it would be possible to couple changes in porosity resulting from swelling and shrinkage. These two factors are incorporated into the theoretical formulations of liquid and vapor flow equations (2) and (3) in section 2.1, respectively.

The simulation results for the cases of introducing the swelling and shrinkage factors are shown in Fig. 8 and 9. Comparison of volumetric water content distribution after 96 and 148 hours, respectively shows that there is a small shift in the amount of water content in the bentonite column

between the two cases. As expected, for the upper end where the swelling is occurred, the value of water content is larger than that of non-swelling case. It should be noted, however, that these expressions are not completely general and may be overly simplified because no distinction is made between connected and total porosity. Other formulations relating porosity and permeability such as power law relation will be also possible. The results obtained are the first attempt of the problem, and indicate that the general approach adopted in this study is valid and worthy of further development. Experimental work on the variation of porosity due to the swelling and shrinkage in unsaturated bentonite is required to gain further confidence.

4. Conclusions

From a mechanistic approach, a potential-based coupled heat, moisture and air transfer model in unsaturated soil is theoretically and numerically formulated. The isothermal and thermal infiltration tests are simulated numerically in one-dimensional spatial domain to compare with the model results. The discrepancy of water uptake was found in the upper region of bentonite sample under isothermal condition. This indicated that air pressure was built up in the bentonite sample which could retard the infiltration velocity of liquid. In a repository it is anticipated that the threshold value at which air escapes will be greater as a result of a greater head of water surrounding the entrapped air. The effect of the air pressure will then be to retard the infiltration rate. Its influence is therefore of major significance since it is a factor that will determine the length of time taken by the repository to reach fully saturated conditions. In order to consider the swelling phenomena of compacted bentonite which cause the discrepancy of the distribution of water content and

temperature, swelling and shrinkage factors were incorporated into the finite element formulation. It was found that these factors could be effective to represent the moisture diffusivity and unsaturated hydraulic conductivity due to volume change of bentonite sample.

The improved correlation between numerical and experimental results is achieved by considering the air and soil swelling effects. However, experimentally and theoretically, further studies are required to resolve the problem of concern. In particular, as the developed program uses large sets of parameters, sensitivity and uncertainty studies would be helpful to pin down the most important parameters so that the further experimental effort could be concentrated on those parameters. The numerical program could be extended to simulate two- or three-dimensional domain. This will allow improved prediction of the final state of a bentonite buffer after the thermal transient in the repository. In addition, it would be possible to apply this program for the assessment of gas migration in low-level radioactive waste repository.

References

1. J.R. Philip and D.A. de Vries, Moisture Movement in Porous Materials Under Temperature Gradients, Trans. Am. Geophys. Union, 38, 222-232 (1957).
2. J. G. Hartley, Coupled Heat and Moisture Transfer in Soils : A Review, Advances in Drying, Vol. 4, Ed. A. S. Mujumdar, Hemisphere Publishing Corp. (1987).
3. D. W. Pollock, Simulation of Fluid Flow and Energy Transport Processes Associated With High-Level Radioactive Waste Disposal in Unsaturated Alluvium, Wat. Res. Res., 22, 5, 765-775 (1986).
4. H.R. Thomas and M.R. Sansom, Coupled

Heat, Moisture and Air Transfer in Unsaturated Soil, Temperature/Capillary Potential Variations in Unsaturated Soil., ASCE, J. Eng. Mech., 121(3), 392-405 (1995).

5. J. Ewen and H. R. Thomas, Heating Unsaturated Medium Sand, Geotechnique, 39(3), 455-470 (1989).

6. S. Takeuchi et al., Water Retention Curve, Water Diffusivity and Water Movement of Compacted Bentonite, J. Geol. Eng. Soc. Japan, 35(3) 129-137 (1995).

7. T. Kanno et al., Moisture Movement Under a Temperature Gradient in Highly Compacted Bentonite, Eng. Geol., 41, 287-300 (1996).

8. Y. Ohnishi and A. Kobayashi, Coupled Analysis on Thermo-Mechanical-Hydrolic Behaviours within Buffer Materials, Proc. the Research Group on Radioactive Waste Management, RWM-87009, 95-105 (1987).

9. M. Nakano et al., Infiltration and Expansive Pressure in the Confined Unsaturated Clay, Trans. JSIDRE, 55-66 (1984).